OPEN ACCESS

University of Dundee

University of Dundee

Biomimetic biohybrid nanofibers containing Bovine Serum Albumin as a bioactive moiety for wound dressing

Homaeigohar, Shahin; Monavari, Mahshid; Koenen, Benedikt; Boccaccini, Aldo R.

Published in:
Materials Science and Engineering: C

DOI:
10.1016/j.msec.2021.111965

Publication date:
2021

Licence:
CC BY-NC-ND

Document Version
Publisher's PDF, also known as Version of record

Link to publication in Discovery Research Portal

Citation for published version (APA):
Homaeigohar, S., Monavari, M., Koenen, B., & Boccaccini, A. R. (2021). Biomimetic biohybrid nanofibers containing Bovine Serum Albumin as a bioactive moiety for wound dressing. *Materials Science and Engineering: C*, *123*, [111965]. https://doi.org/10.1016/j.msec.2021.111965

General rights
Copyright and moral rights for the publications made accessible in Discovery Research Portal are retained by the authors and/or other copyright owners and it is a condition of accessing publications that users recognise and abide by the legal requirements associated with these rights.

• Users may download and print one copy of any publication from Discovery Research Portal for the purpose of private study or research.
• You may not further distribute the material or use it for any profit-making activity or commercial gain.
• You may freely distribute the URL identifying the publication in the public portal.

Take down policy
If you believe that this document breaches copyright please contact us providing details, and we will remove access to the work immediately and investigate your claim.

Download date: 04. May. 2023

Materials Science & Engineering C 123 (2021) 111965

Contents lists available at ScienceDirect

Materials Science & Engineering C

journal homepage: www.elsevier.com/locate/msec

Biomimetic biohybrid nanofibers containing bovine serum albumin as a bioactive moiety for wound dressing

Shahin Homaeigohar [a,b,*], Mahshid Monavari [a], Benedict Koenen [a], Aldo R. Boccaccini [a]

[a] Institute of Biomaterials, Department of Materials Science and Engineering, University of Erlangen-Nuremberg, 91058 Erlangen, Germany
[b] School of Science and Engineering, University of Dundee, Dundee DD1 4HN, United Kingdom

ARTICLE INFO

Keywords:
Protein
Polycaprolactone
Biohybrid
Electrospinning
Wound dressing

ABSTRACT

For the first time, a biohybrid nanofibrous wound dressing is developed via green electrospinning of a blend solution of bovine serum albumin (BSA) (1 and 3 wt%) and polycaprolactone (PCL). In such a system, the components are miscible and interact through hydrogen bonding between the carbonyl group of PCL and the amine group of BSA, as verified by ATR-FTIR. As a result, the biohybrid nanofibers show a superior elastic modulus and elongation (300% and 58%, respectively) compared with the neat PCL nanofibers. The included protein induces a hydrophilicity effect to the PCL nanofibers, notably at the higher BSA content (3 wt%). In contrast to the neat nanofibers, the biohybrid ones are bioactive and encourage formation of biominerals (made of amorphous calcium carbonate) on the surface, after immersion in simulated body fluid (SBF). Based on the WST-8 cell viability tests, NIH3T3 fibroblast cells were seen to properly interact with the biohybrid mats and to proliferate in their proximity. SEM images show that the cells largely adhere onto such nanofibers even more than they do on the neat ones and adopt a flattened and stretched shape. In addition, the live/dead assay and phalloidin/DAPI staining assay confirm large cell viability and normal cell morphology on the biohybrid nanofiber mats after 4 days incubation. Taken together, BSA/PCL nanofibers are able to offer optimum mechanical properties (elasticity) as well as mineralization which can potentially stimulate the wound healing process, and can be considered a suitable candidate for wound dressing applications.

1. Introduction

Biomimicry or biomimetics is related to the nature-inspired development of new artificial systems. This goal is mainly achieved through simulating the microstructure-induced macrofunction of biomaterials [1]. Such an inspiration has been largely taken into account by researchers in the field of biomedical engineering for construction of tissue engineering scaffolds, wound dressings, etc. [2,3]. Extracellular matrix (ECM), i.e. the acellular constituent of tissues, functions as a scaffold that holds the cells physically and enables them to actively proliferate, migrate, and differentiate [4]. ECM comprises an amorphous complex of proteins (collagen, mainly) and polysaccharides, whose interplay leads to the establishment of an interconnected nano- or micro-fibrous network [5]. Additionally, the protein fibrillar structure provides a plethora of cell adhesive peptide moieties facilitating cell anchorage [6]. Imitating such a biological structure, synthetic and nature-derived nanofibrous materials have found large applicability with respect to tissue regenerating scaffolds and wound healing stimulating materials [7–9]. Nanofibrous meshes comprising many intersecting nanofibers as small as a few microns to a few hundred nanometers can provide a large exposed surface area and nanoporosity, thereby facilitating interaction with the cells available in the damaged tissue or the wound bed through an ECM mimicking structure [10].

While the nature-derived polymers are typically bioactive and drive cell-matter interactions, synthetic polymers suffer from poor biocompatibility unless are hybridized with biologically active components [11]. In addition to biomimetics, biointegration, i.e. incorporation of natural organic materials into synthetic materials, has also advanced in the past few decades and is emerging as an important concept in biomedical materials technology [1]. This field deals with integration of bioactive components including proteins and living cells into synthetic materials [1], in order to further simulate the biological materials' biochemistry. While a nanofibrous architecture biomimics the ECM in terms of topography and nanostructure, the presence of biologically recognizable additives provides the cells with the required biochemical cues. This feature promotes biocompatibility and bioactivity of the

* Corresponding author at: School of Science and Engineering, University of Dundee, Dundee DD1 4HN, United Kingdom.
E-mail address: shomaeigohar001@dundee.ac.uk (S. Homaeigohar).

https://doi.org/10.1016/j.msec.2021.111965
Received 7 October 2020; Received in revised form 6 February 2021; Accepted 8 February 2021
Available online 12 February 2021
0928-4931/© 2021 The Authors. Published by Elsevier B.V. This is an open access article under the CC BY-NC-ND license (http://creativecommons.org/licenses/by-nc-nd/4.0/).

scaffold, which should accelerate regeneration of the lost tissue.

Applying the principles of biomimetics and biointegration, here, we devise a state of the art nanofibrous wound dressing that enjoys a biodegradable biohybrid formulation. Biodegradable polymers have drawn large interest for biomedical applications and specifically for the construction of nanofibrous wound dressings. These polymers are derived from a natural origin such as polysaccharides and cellulose [12–15] or are synthetic, e.g. polyesters, polyanhydrides, polyphosphazenes, polyurethane, and poly (glycerol sebacate) [16,17]. Among the synthetic biodegradable polymers, polycaprolactone (PCL) is a popular inexpensive, bioresorbable and biocompatible polymer that has been widely researched as a wound dressing material since the 1970s [18]. As a result, different wound dressings made of PCL as ultrathin films (treated with NaOH and fibrin [19] or blended with chitosan and reinforced by clay and curcumin [20]), 3D printed patches based on PCL filaments [21], and 3D printed meshes (containing tricalcium phosphate) [22] have been developed. PCL has been also copolymerized with polyethylene glycol (PEG) and aniline trimer to result in robust, electroactive polyurethane-urea film wound dressings [23]. Extensive in vitro and in vivo testing has confirmed the promising applicability of this polymer for biomedical applications, leading to FDA approval for a variety of medical and drug delivery systems made thereof [24]. Recently, PCL nanofibers have been employed in production of tissue engineering scaffolds [25–28] and wound dressings [29,30]. Despite favorable characteristics of PCL for biomedical applications, its hydrophobicity [31], lack of cellular recognition sites, poor bioactivity as well as relatively low mechanical strength and elongation [32] are important bottlenecks hindering further use of this interesting polymer in biomedicine. Accordingly, addressing such shortcomings has been targeted in many relevant researches. For instance, blending of PCL with hydrophilic biopolymers has been proved efficient in enhancement of cellular activity [33,34] and stretchability [35]. In addition, inclusion of reinforcing inorganic nanofillers made of e.g. bioglass [36], calcium phosphate [37], forsterite [38], silica nanoparticles [39], carbon nanotube [40], etc. has led to improvement of mechanical properties.

In the current study, we develop a new nanofibrous wound dressing based on PCL nanofibers. To fulfil optimum bioactivity and desired mechanical properties, we benefit from bovine serum albumin (BSA) as a blending agent or filler. The BSA protein is a commercial, inexpensive biomacromolecule, derived from cow blood, a widely available byproduct of the cattle industry. The combination of PCL and BSA protein is proposed to enhance physicochemical properties as well as bioactivity of the nanofibrous wound dressing made thereof. Implementing the advanced concepts of biomimetics and biointegration, the as-developed system will show various merits for new generation of nanostructured wound dressing materials. The biohybrid nanofibers are produced through electrospinning and based on using benign solvents such as formic acid and acetic acid. This eco-friendly, simple, scalable production method coupled with the inexpensive materials employed in our approach notably raises the chance of large-scale production and industrialization of the resulting product.

2. Materials and methods

2.1. Materials

PCL with the molecular weight (M_n) of 80 kDa (440744, CAS No. 24980-41-4) and BSA with the molecular weight of 66,430 (A2153, dried powder, CAS No.9048-46-8) were purchased from Sigma Aldrich (Munich, Germany). Acetic acid (AA) and formic acid (FA) were obtained from VWR (Darmstadt, Germany). All the materials were used as received.

2.2. Sample preparation

The BSA/PCL nanofibers were produced via electrospinning of PCL and BSA/PCL solutions. A PCL solution (11 wt% in AA/FA (1:1 (v/v))) was used for preparation of the electrospun PCL nanofibers. To synthesize the BSA/PCL nanofibers, BSA (1 and 3 wt% of the PCL amount) was co-dissolved in the above-mentioned PCL/AA/FA solution and stirred for a sufficiently long time. Eventually, the as-prepared solutions were used for electrospinning and production of the respective nanofiber mats. For the purpose of electrospinning, a commercial electrospinning setup (IME Medical Electrospinning, Waalre, The Netherlands) was employed. The setup was equipped to a climate-controlled chamber (EC-CLI) and a gas shield accessory. The solution compositions and electrospinning parameters for the different classes of nanofibers are tabulated in Table 1.

2.3. Characterization of structural properties

2.3.1. Nanofiber morphology and diameter

Morphological characteristics of the nanofibers were determined via SEM analysis (FE-SEM, Auriga, Carl-Zeiss, Jena, Germany). Before the analysis, all the samples were sputter coated with gold. The ImageJ software (NIH, Bethesda, MD, USA) was used to determine the average diameter of 20 randomly selected nanofibers. The histogram graphs for nanofiber diameters were drawn based on the 20 measured diameters by the Origin software.

2.3.2. EDX analysis

The presence and distribution mode of BSA within the PCL nanofibers were tracked by using energy dispersive spectroscopy (EDS) (Oxford Instruments, Abingdon, UK) under a 20 kV applied voltage.

2.3.3. Porosity and pore size measurement

To quantify the porosity of the nanofibrous mats, 3 circular pieces were cut and their radius (area), thickness, and mass were precisely determined by a vernier caliper, a digital micrometer (Deltascope® MP2C from Fischer), and an electronic balance (with the resolution of 0.1 mg), respectively. The nanofibrous mats' apparent density (ρ) was calculated based on the measured mass and volume and was correlated to the porosity of the mats through Eq. (1) [41]:

$$\varepsilon = \frac{(\rho_0 - \rho)}{\rho_0} \times 100\% \quad (1)$$

where ε is porosity and ρ_0 is the average density of the main components of the nanofibers, BSA and PCL, that can be calculated according to Eq. (2) [41]:

$$\frac{1}{\rho_0} = \frac{\phi_{PCL}}{\rho_{PCL}} + \frac{\phi_{BSA}}{\rho_{BSA}} \quad (2)$$

where ρ_{PCL} and ρ_{BSA} are 1.135 [42] and 0.996 g/cm^3 [43], respectively. ϕ_{PCL} and ϕ_{BSA} are mass fractions of the components. Porosity of the BSA/PCL nanofiber mats was also determined by the ImageJ software to compare with that obtained through Eq. (1).

Applying the nanofiber diameters, d (nm) and porosities, ε (–) into Eq. (3), the mean pore radius ($\bar{r}$) of the nanofibrous mats can be determined [44]:

$$\bar{r} = \frac{\sqrt{\pi}}{4}\left(\frac{\pi}{2log\left(\frac{1}{\varepsilon}\right)} - 1\right)d \quad (3)$$

2.3.4. Mechanical properties

A standard uniaxial tensile test machine (Instron, Darmstadt, Germany) was employed to determine the mechanical properties of the nanofiber mats. The nanofibrous scaffolds were cut by a surgical blade as strips of 3 × 25 mm and fixed in paper frames. The testing parameters were: an initial length of 25 mm, a 100 N cell load, and the elongation

Table 1
The conditions of solution preparation and electrospinning for the BSA/PCL nanofibers.

Composition	Solution			Electrospinning					
	PCL conc. (wt %)	BSA conc. (wt %)	Stirring time (h)	Feed rate (ml/h)	Collecting distance (cm)	Voltage (kV)	Temperature (°C)	Time (h)	Relative humidity (%)
PCL	11	0	3	0.4	11	15	25	3	40
BSA/PCL 1	11	1	3	0.4	11	15	25	3	40
BSA/PCL 3	11	3	5	0.4	11	20	25	3	40

rate of 1 mm.min^{-1} for the elastic area, followed by that of 10 mm.min^{-1} in the plastic region. Young's modulus (E), tensile strength, and elongation were obtained from stress–strain curves. Averages values and standard deviations (SDs) were determined after the test of at least three specimens of each composition.

2.3.5. Hydrophilicity measurement

Hydrophilicity of the nanofiber mats was determined by a water contact angle measurement instrument (DSA 30, Krüss, Germany) and after depositing a 3 μl water droplet on different locations of the respective nanofiber mats.

2.3.6. Surface chemical analysis

The surface chemistry of the nanofibers was probed through Fourier transform infrared attenuated total reflectance spectroscopy (IRAffinity-1S, Shimadzu Corporation, Kyōto, Japan). In this regard, 40 spectral scans were averaged throughout the spectral range of 4000–400 cm^{-1} with the resolution of 4 cm^{-1} at room temperature.

2.3.7. Phase composition and crystallinity analysis

The crystallinity and phase composition of the neat and biohybrid nanofibers were characterized by X-ray diffraction (XRD) analysis using a diffractometer (Miniflex 600 HR, Rigaku, Japan). Data were collected over a 2θ range from 20° to 40° with a step size of 0.02.

2.3.8. Wound exudate removal

Wound exudate absorption potential of the nanofibrous wound dressings was determined via a water-uptake test and calculated using Eq. (4):

$$Water\ uptake\ capacity\ (\%) = \frac{W_t - W_0}{W_0} \times 100 \quad (4)$$

where W_0 is the weight of the nanofiber mat in the dry state and W_t is the momentary weight of the nanofiber mat after immersion in phosphate-buffered saline (PBS) at the room temperature for given time intervals up to 24 h. The average value of water uptake capacity for three nanofiber mats was reported.

2.3.9. Water vapor permeability

The water vapor permeability of the nanofibrous dressing was measured according to ASTM E96 standard. To solely investigate the effect of composition and exclude the error factor of large pore size, only PCL and BSA/PCL (1 wt%) nanofiber mats were considered for this measurement and compared. For this test, the nanofibrous mats were fixed onto the mouth (with the area of 176 × 10^{-6} m^2) of 5 ml storage vials with screw caps. The vials were filled with 4 ml of distilled water and the assembly was placed in a shaking incubator at 37 °C for 24 h. At different intervals, the whole vial was weighed and the water vapor transmission rate (WVTR) was calculated using Eq. (5) [45]:

$$WVTR = \frac{\Delta W}{t \times A} \quad (5)$$

where ΔW represents the change in the weight of water (g), A is the permeation area (m^2), and t is the time (duration) thereafter the weight change is recorded. For this measurement, the average value of WVTR for three nanofibrous mats was reported.

2.3.10. Degradation of the nanofibers

To evaluate the degradation level of the nanofibrous dressings, they were submerged in individual bottles containing 10 ml of PBS (at pH 7.4). The bottles were placed in a shaking incubator for a time period of up to 3 months at 37 °C. Afterwards, the nanofibrous dressings were removed, washed thoroughly with deionized water, and eventually air dried. The morphology of the degraded samples was recorded using SEM.

2.4. Characterization of biological properties

2.4.1. Acellular bioactivity effect

The bioactivity of the BSA/PCL nanofiber mats was evaluated by immersing them in SBF, prepared according to the protocol of Kokubo et al. [46], for 3 days at 37 °C and under neutral pH and monitoring the formation of biominerals on the surface via SEM, XRD and EDX.

2.4.2. Cell viability test

The nanofiber mats were cut as 1 × 1 cm^2 squares using a surgery blade. Subsequently, the nanofiber samples were sterilized under UV for at least 1 h. The as-sterilized nanofiber samples were challenged in terms of NIH 3T3 cell viability. For this purpose, the nanofiber mats were fixed in the CELLCROWN 24 scaffold holders (Scaffdex Oy, Tampere, Finland) and mounted into several wells of a 24-well plate. Each nanofiber mat was seeded with 3 × 10^5 NIH 3T3 cells re-suspended in their standard culture medium i.e. Dulbecco's modified eagle medium (DMEM) containing 10% fetal bovine serum (FBS) and 1% antibiotic (penicillin and streptomycin) (500 μl). The nanofibers co-cultured with the cells were incubated in a humidified atmosphere of 95% air and 5% CO_2 at 37 °C for 1 and 4 days. After each interval, cell viability was determined through the WST-8 assay (Sigma Aldrich). The cell morphology was also imaged by SEM after fixing the cells by a 4% paraformaldehyde solution and permeabilizing them by a 1% Triton X-100 solution.

2.4.3. Live-dead assay

Viable and dead cells were identified through the live/dead assay (L3224, Invitrogen). For this purpose, the cells were stained by 200 μl of calcein AM (2 μM in PBS) and DAPI (4 μM in PBS) at room temperature for 30 min. Subsequently, they were monitored and imaged by a fluorescence microscopy (Axio Observer D.1, Carl Zeiss MicroImaging GmbH). It is worthy to note that DAPI was employed to visualize the dead cells according to a specific live-dead assay protocol established at our institute, replacing propidium iodide that might falsely stain the live cells permeabilized by residual trypsin, as well.

2.4.4. Actin and nuclei staining assay

The fibroblast cells were first washed with DPBS (Dulbecco's Phosphate Buffered Saline (Gibco, UK)) and then fixed by formaldehyde (3.8% v/v) for 15 min at the ambient temperature. After fixation, the cells were washed with DPBS and subsequently permeabilized for 5 min (using Triton X-100 (0.1% v/v) and Sucrose (5.0% w/v)). Later, the cells were subjected to rhodamine–phalloidin (8.0 μl/ml) (Invitrogen, USA) for 1 h at the ambient temperature and eventually were washed with DPBS. Nuclei staining was performed by exposure of the cells to DAPI

(1.0 μl/ml) (Invitrogen, USA) for 5 min. The stained cells were imaged by a fluorescence microscopy (Axio Observer D.1, Carl Zeiss Micro-Imaging GmbH).

2.5. Statistical analysis

The measurements were expressed as mean ± standard deviation. Statistical analysis of the biological data was conducted by one-way analysis of variance (ANOVA) and the Tukey test. In such analyses, a confidence level of 95% ($p < 0.05$) was considered to show significant differences.

3. Results and discussion

3.1. Nanofiber characteristics

The morphology of the PCL and BSA/PCL nanofibers is demonstrated in Fig. 1a–c. The PCL and BSA/PCL nanofibers are beadles with a uniform diameter distribution. The nanofiber diameter notably grows at the highest BSA concentration. While the PCL and 1 wt% BSA/PCL nanofibers are 140–160 nm in diameter, the 3 wt% BSA/PCL nanofibers' average diameter rises to 400–500 nm. Histograms of the nanofibers diameter are shown in Fig. 1d–f. Growth of the nanofibers' diameter is attributed to enhancement of viscoelastic force at the largest protein concentration that opposes against electrical repulsion force and further stretching of the polymer jet. SEM images also show that in contrast to the neat nanofibers, the biohybrid nanofibers are curvy. This implies that they have undergone larger bending instability [47], due to their higher net charge density in the presence of the protein, getting protonated in the solution. Interestingly, a web like structure with fine nanofibers forms within the 3 wt% BSA/PCL nanofiber mat. Formation of such a secondary structure relates to jet splitting during electrospinning and instability of the droplet on the tip of the spinneret caused by the high viscosity of the BSA/PCL solution. A similar behavior has already been reported by Sambudi et al. [48] for chitosan/PVA electrospun nanofibers.

Porosity of the nanofiber mats is of high importance, given its impact on exudate uptake capacity, water vapor permeability and cell interaction with the nanofibrous structure. The nanofiber diameter and curvy or straight alignment of the nanofibers are determining factors on porosity and pore size of the nanofiber mats.

Fig. 2a shows that the nanofibrous mats are highly porous and their porosity ranges from 89, 94 and 96%, for the PCL and 1 wt% and 3 wt% BSA/PCL nanofiber mats, respectively. Witnessed by the SEM images (Fig. 1a–c), the biohybrid mats are slightly more porous, partly attributed to their curvy nanofibers. To further validate the porosity values measured via Eqs. (1) & (2), three SEM images of the nanofiber mats were also analyzed in terms of porosity by using the ImageJ software. The results are shown in Fig. S1 and imply a large difference with those determined experimentally. According to the image analysis, the PCL and biohybrid nanofiber mats possess 58% and 61.5–62.5% (for those containing 1 and 3 wt% BSA, respectively) porosity. However, these porosity values are hardly reliable, owing to this reality that the selected image represents only a partial 2D anisotropic surface and is unable to precisely consider the 3D porous structure of the whole sample. Corresponding with the enhanced porosity of the biohybrid nanofiber mats, as shown in Fig. 2b, pore size also increases from 2050 nm for the PCL nanofiber mat to 4400 nm and 17,400 nm for the biohybrid nanofiber mats with 1 wt% and 3 wt% BSA, respectively. At a given areal density and porosity, larger nanofibers create larger pores [44]. As mentioned earlier, the larger nanofiber diameter of the biohybrid nanofibers stems from interaction between the protein and polymer, i.e. hydrogen bonding (as will be shown later), leading to a higher viscoelastic force opposing against stretching of the polymer jet.

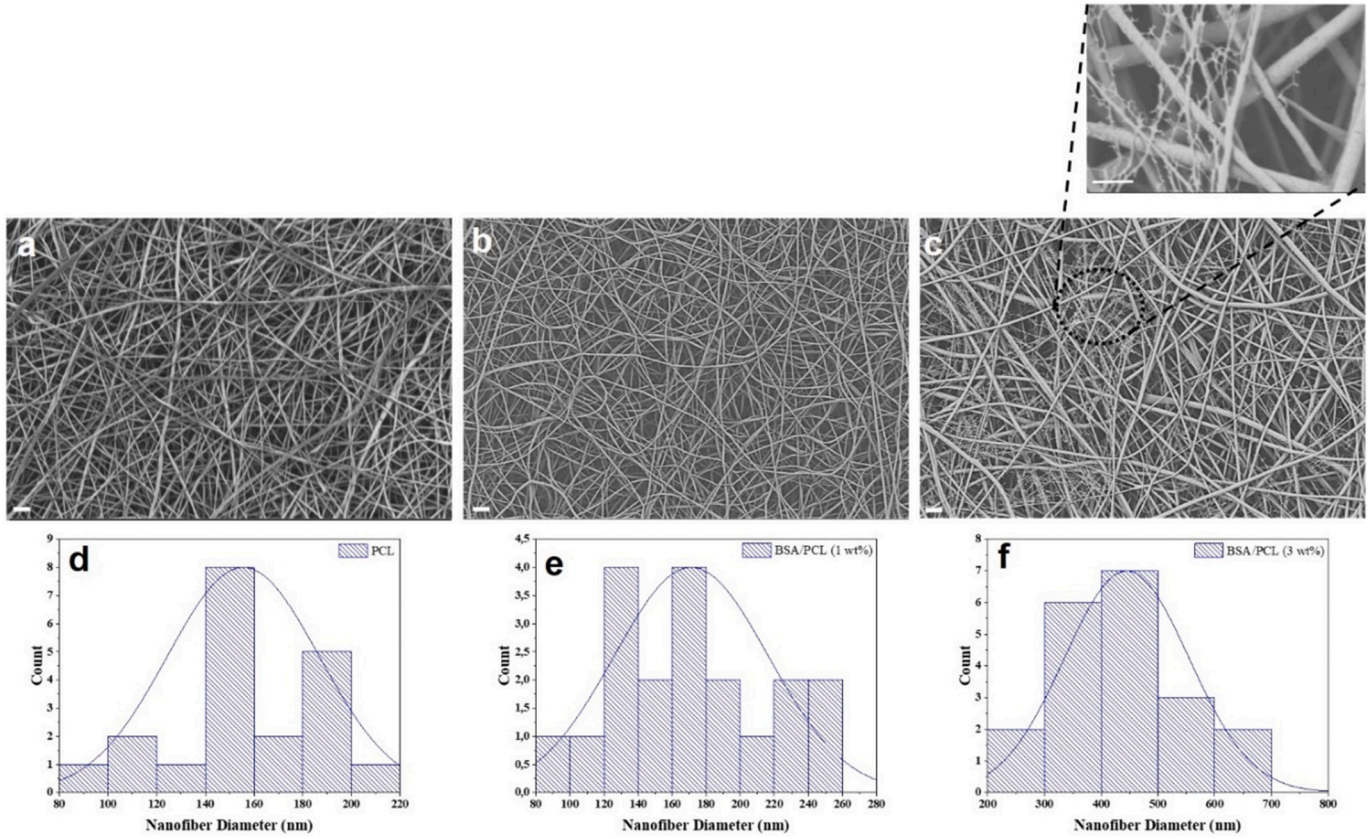

Fig. 1. SEM images of the biohybrid nanofibers containing a) 0 wt%, b) 1 wt%, and c) 3 wt% BSA (the scale bars in a–c and in the inset image in c represent 2 μm and 1 μm, respectively). Histogram of diameter of the biohybrid nanofibers containing d) 0 wt%, e) 1 wt%, and f) 3 wt% BSA.

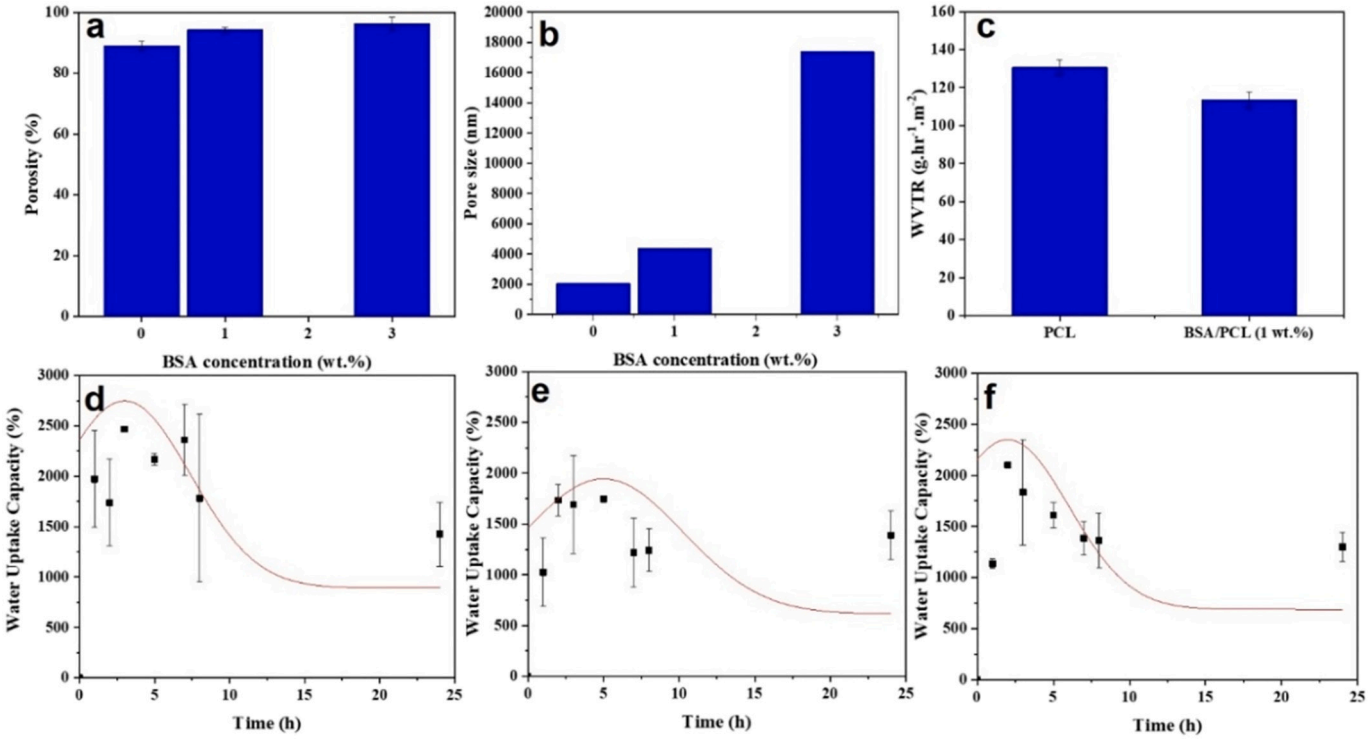

Fig. 2. Structural characteristics of the biohybrid nanofiber mats including a) porosity, b) pore size, c) water vapor transmission rate (WVTR; note that due to significant discrepancy of pore size and porosity between the 3 wt% BSA/PCL nanofiber mat with the two other compositions, notably impacting the water vapor transmission, it was excluded from the measurements). Water uptake capacity of the biohybrid nanofiber mats containing d) 0 wt%, e) 1 wt%, and f) 3 wt% BSA.

As Eichhorn and Sampson [44] state, the distance between nanofibers' crossings ($\overline{g}$) is closely related to the pore size distribution, and can be explained by Eq. (6):

$$\overline{g} \approx \left(\frac{\pi}{4\varphi} - 1\right)\omega \tag{6}$$

According to this equation, the only fiber property that affects the pore size is fiber diameter (ω), and the only mat property that could be influential is the fractional contact area, Φ, which is associated with porosity.

Porosity is a determining factor in performance of a nanofibrous wound dressing, particularly in water vapor permeation and exudate uptake capacity. A proper wound dressing should be permeable to water vapor so that a moist exudate is kept under the dressing without pooling. In fact, the wound dressing must prevent excess fluid absorption and evaporation ending up with desiccation of the wound bed [49]. Fig. 2c shows the water vapor transmission rate for the PCL and 1 wt% BSA/PCL nanofiber mats whose porous structure is comparable. Despite a similar porosity, the biohybrid nanofiber mat is less permeable than the PCL nanofiber mat, implying that surface chemistry and thus hydrophilicity of the biohybrid plays a role in its water vapor permeation behavior. It is assumed that water is condensed on the nanofiber surface and thereby swells the protein component after its conformational change. This hydration induced transformation narrows the pore size and declines the porosity of the mat and challenges further passage of water vapor through the structure. The swelling mechanism of the protein component under the influence of water vapor can be explained as follows: First, small water molecules diffuse into the BSA chain networks and thereby soften or plasticize them and form water bound BSA networks. In such systems, the BSA molecules have notably higher mobility than they had before exposure to the water vapor stream [50]. Second, the water vapor molecules whose temperatures range from 0 to 100 °C transfer thermal energy in different levels to the water bound protein system [50]. Thermodynamically [51], internal energy (E) of a gas system, e.g., water vapor, depends on its temperature (T) and can be determined via the formula: $E = (f / 2)nRT$. In this equation, f is the number of degrees of freedom for the gas molecule (equals to 12 for water vapor), n is the molar number of molecules, and R is the ideal gas constant and equal to 8.314 J/K·mol. In order to keep stable equilibrium, the protein system maximally absorbs the thermal energy of the water vapor molecules. As a result, the BSA–water system's energy level prevails the energy boundary of local vibrations and drives long-range molecular mobility for the BSA–water system. Eventually, the protein chains self-assemble as stacked β-sheet crystals [50]. Accordingly, the protein molecules are swollen on the nanofibers surface, thereby narrowing the pore size and rendering higher steric hindrance for water vapor permeation. On the other hand, induced by progressive protein's conformational change and high mobility of the protein molecules, a larger number of polar functional groups become exposed on the nanofibers surface. Such binding groups encourage further penetration of water molecules into the structure and expansion of the nanofibers. A similar behavior has been reported by Elbahri et al. [52–54] for a BSA/PANGMA nanofiber material, wherein the protein segment is swollen upon hydration and thereby lowers the porosity.

In terms of exudate (here simulated by PBS) uptake capacity, as seen in Fig. 2d–f, the PCL nanofiber mat shows a larger capacity than the biohybrid nanofiber mats. Upon wetting, the biohybrid nanofibers become swollen, thanks to the presence of protein and its hydration induced expansion effect, leading to loss of specific surface area and porosity. Having a larger porosity and interfiber spacing that is not notably sacrificed by the protein swelling, the 3 wt% BSA/PCL nanofiber mat encompasses (absorbs) more liquid (exudate) than does the other biohybrid composition. All the nanofiber mats reach the saturation level in less than 3 h. Their hydrophobic nature (excluding the 3 wt% BSA/PCL nanofibers, as will be shown later) and the presence of air pockets between the nanofibers resist against full saturation in a short time (instantly). After reaching the maxima, the nanofiber mats start to lose their capacity, most likely due to their swelling and porosity loss. After a

given time (7 h), an equilibrium in exudate uptake capacity is reached and is maintained until the end of the test course, reflected as a plateau.

The uniform distribution of BSA across the biohybrid nanofiber mat was validated by EDX analysis. Fig. S2 shows elemental mapping of the surface of 3 wt% BSA/PCL nanofiber mat, wherein the sulfur atoms are highlighted by green spots throughout the mat. Sulfur originates from the thiol groups in BSA's cysteine residues and plays an important role in formation of disulfide bonds, essential for folding, activity, and stability of BSA [55]. The presence of the BSA protein and its likely interaction with PCL were further tracked by ATR-FTIR. As shown in Fig. 3a, the peaks emerging at 1650 cm^{-1} and 1530 cm^{-1} are the vibration peaks of amide I and amide II groups in the BSA molecules [56]. This distinct feature clearly implies successful blending of BSA with PCL and emergence of the polar functional groups related to BSA that can end up with a higher hydrophilicity of the biohybrid nanofibers, Fig. 3b. The main characteristic peaks of PCL appear in the region of 1250–1450 cm^{-1} attributed to symmetric C—H stretching and C—C stretching. Furthermore, the C═O bond (stretching vibrations of the carboxyl) and C—O groups of PCL appear at 1750 cm^{-1} and within 1122–1250 cm^{-1} region, respectively. More precisely, C—O stretching is represented by a peak at 1122 cm^{-1} and stretching vibrations of the ether groups (C-O-C) by the peaks emerging at 1175 and 1240 cm^{-1} [57–59]. Many of these peaks undergo a shift and loss of intensity, as witnessed for C—O, C-O-C and C═O groups, marked by a blue triangle. Such changes stress formation of a secondary bonding, e.g. hydrogen bonds between the two main components of the biohybrid system.

The physical interaction (hydrogen bonding and molecular entanglements) between the BSA and PCL components is believed to end up with a more robust, stiff nanofibrous structure. As shown in Fig. 3c, the hydrogen bonding taking place between the respective functional groups of the protein (amine) and polymer (carbonyl) phases, challenges molecular mobility when subjected to mechanical stress. As a result, elastic modulus of the biohybrid nanofibers notably rises (170% and 200% for 1 and 3 wt% BSA concentrations, respectively, compared to the PCL nanofibers).

Interestingly, the biohybrid nanofibers can be stretched much larger than the PCL nanofibers before rupture, Fig. 3d. A comparable mechanical behavior has been reported by Aghdam et al. [60] for a polyglycolic acid (PGA)/PCL nanofiber system and Wan and Chen [61] for a GO reinforced PCL nanofiber material. It is assumed that the protein and/or polymer component could be crystallized while the nanofiber is stretched (as will be discussed and validated later) and crystallinity contributes to the higher elongation at break. Additionally, the larger unfolding extent of amorphous random coils of BSA could lead to a higher elongation at break for the biohybrid nanofibers [62]. Fig. 3e shows that the biohybrid nanofiber mat containing 1 wt% BSA exhibits higher resistance to tensile stresses in comparison to the other compositions investigated. This biohybrid nanofiber mat is followed by the neat PCL nanofiber mat in terms of tensile strength. While due to the nature of the application, this mechanical feature could be of less importance compared to elastic modulus, it is interesting to ponder the mechanical behavior of the biohybrid nanofiber mats at a high level of stress. If nanofiber diameter and closeness of the molecular chains in a confined area are taken into account, the BSA (1 wt%)/PCL nanofibers and PCL nanofibers should be compared with each other. In this regard, it is evident that BSA is playing a notable role and due to cross-linking of PCL chains it improves their resistance against failure, reflected in the fibers' higher tensile strength. However, at the larger BSA concentration, the biohybrid nanofibers seem to fail sooner, most likely due to their large fiber diameter that allows the polymer chains and protein

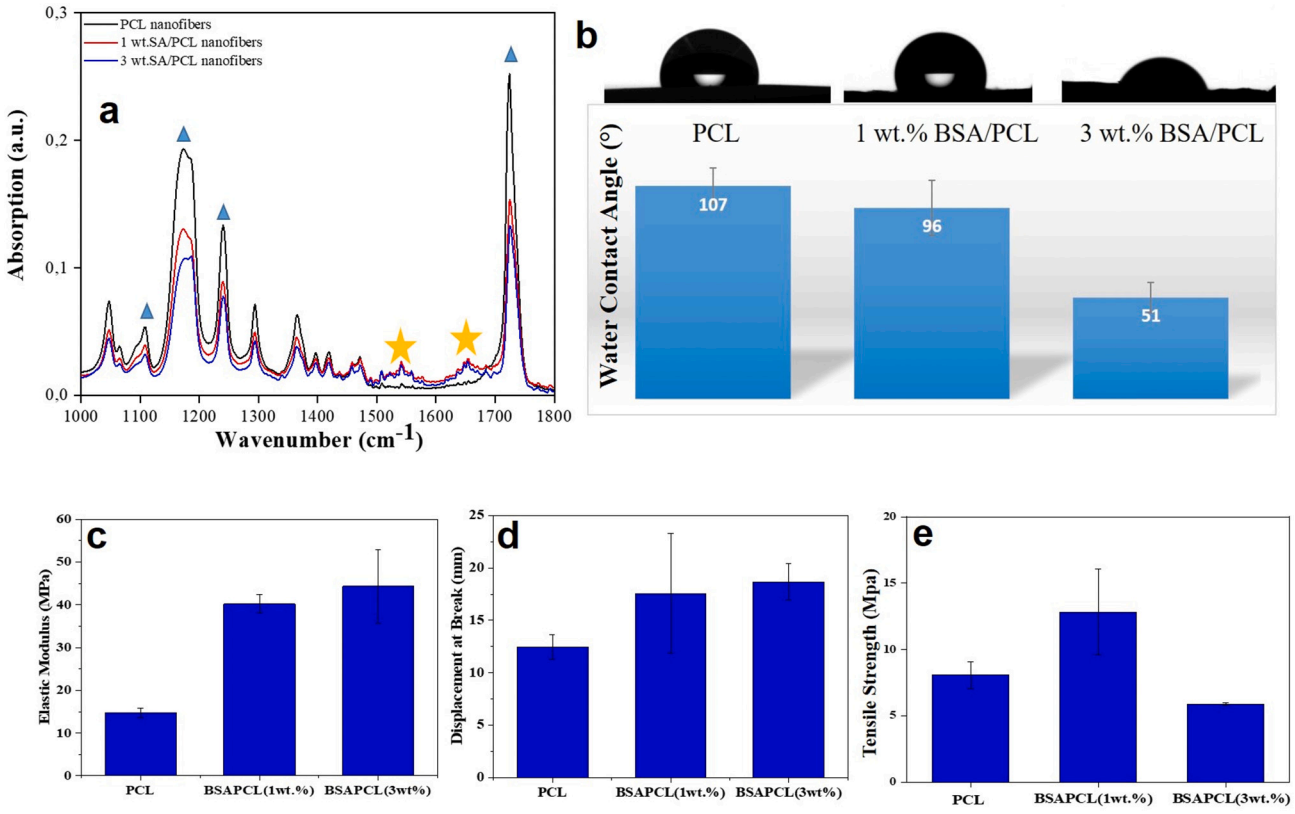

Fig. 3. Physicochemical characteristics of the biohybrid nanofiber mats. a) ATR-FTIR spectra imply emergence of the protein characteristic peaks (the amide I and II peaks have been marked with the yellow stars) and a slight shift (marked with the blue triangles) of several characteristic peaks of PCL, indicating formation of hydrogen bonds between PCL and BSA functional groups. b) Water contact angle measurement for the nanofiber mats before and after incorporation of BSA. c) Elastic moduli, d) displacement at break, and e) tensile strength for the biohybrid nanofiber mats versus the PCL nanofiber mat. (For interpretation of the references to color in this figure legend, the reader is referred to the web version of this article.)

molecules to stay away from each other, thereby lowering the entanglement and intermolecular bonding, remaining less ordered and oriented and capable to move freely.

An appropriate dressing material should be elastic, pliable, and mechanically robust to avoid further damage of the wounded tissue [63]. A wound dressing's mechanical properties also influence cellular behavior, given the correlation of cell-matter interactions with the imposed shear stresses and mechanical signaling channels that govern the cell migration, proliferation, and differentiation [64]. Thus, for a wound dressing application, mechanical properties of the dressing material must suit the beneath skin tissue's to create analogous biomechanical signals [62]. As reported in the literature [65], the human skin's tensile elastic modulus varies from 0.1 to 10 MPa. The elastic modulus of the BSA/PCL nanofibrous dressing can reach up to ~40 MPa, that significantly exceeds this range. However, presumably when the nanofiber mat is wetted by the wound liquids, this stiffness would majorly drop down to the level of natural skin tissue's. Water molecules can disrupt the hydrogen bonds, thereby declining the stress transfer between polymer chains and permit them move relative to each other when tensile stress is applied [66,67]. In addition to optimum elasticity, high elongation of a wound dressing material is of importance to hinder the disruption of wound-bed during wound closure/contraction, to maintain the structural cohesion and to ease the barrier functions [68]. Thanks to their superior stretchability, this prerequisite is totally met by the biohybrid nanofibrous dressing developed in our study.

A more profound mechanical stability is also reflected in the hydrolytic degradation behavior of the biohybrid nanofiber mats. While after one month the PCL nanofiber mat seems partially degraded with some eroded parts (Fig. 4a), the biohybrid nanofiber mats are almost intact (Fig. 4b & c). The only visible change seen in the 3 wt% BSA/PCL nanofiber mat could be related to the salt precipitates spread across the mat. The degradation extent of the PCL nanofibers reaches its maximum after three months, when the nanofibers have been crumpled and converted to spheres and a major fraction of the nanofiber mass has vanished, Fig. 4d. Interestingly, even after three months immersion in PBS, the biohybrid nanofiber mats are still defect free (Fig. 4e & f). While, as mentioned earlier, the biohybrid nanofiber mats could partly lose their superior elastic modulus in water due to the disruption of hydrogen bonds, PBS can provide the medium with ions that could stabilize the structure of the biohybrid nanofibers. The ionic interaction between PBS (its electrolytes) and the biohybrid's constituent materials or provision of the ions that could act as cross-linker for the protein-protein and/or protein-polymer couples are the main strengthening mechanisms [65]. A similar behavior has been reported for the nanocellulose-polyethylene glycol (PEG) bionanocomposites that have achieved a higher elastic modulus after immersion into PBS [65]. This behavior has been found to be affected by the interaction of ions present in the PBS solution and the oxidized cellulose nanofibrils.

The BSA/PCL nanofibers are assumed to act in a hydration responsive manner. The BSA domains that are primarily as folded (α-helix) in the dry state would expand upon exposure to aqueous medium and be transformed to an unfolded structure (β-sheet). The expanded protein structure provides a larger number of functional groups and thus would be more interactive with the external environment, e.g. cells, and confers the encompassing material with a higher bioactivity, Fig. 5a.

Formation of a calcium rich shell on the biohybrid nanofibers upon immersion in the SBF solution is closely associated with their biological activity and enhanced cell-matter interactions [69,70]. In our previous study [9], we validated that formation of a hydroxyapatite coating on the biofunctionalized polyacrylonitrile (PAN) nanofibers leads to higher viability for fibroblast cells as well as keratinocytes. With such a preassumption, the BSA/PCL nanofibers were immersed in a SBF solution with the ionic composition tabulated in Table S1. As shown in Fig. 5b–g, other than the PCL nanofibers that are unable to biomineralize, the biohybrid nanofiber mats are almost entirely covered by a whitish biomineral layer. Nucleation of the biominerals takes place on the protein functional groups, Fig. 5h, widely exposed after hydration of the material (protein) and when pH is above the protein's isoelectric point. It is worthy to note that under the isoelectric point of BSA, i.e. 4.7 [53,71], the protein's secondary structure is α-helix and the tryptophan and

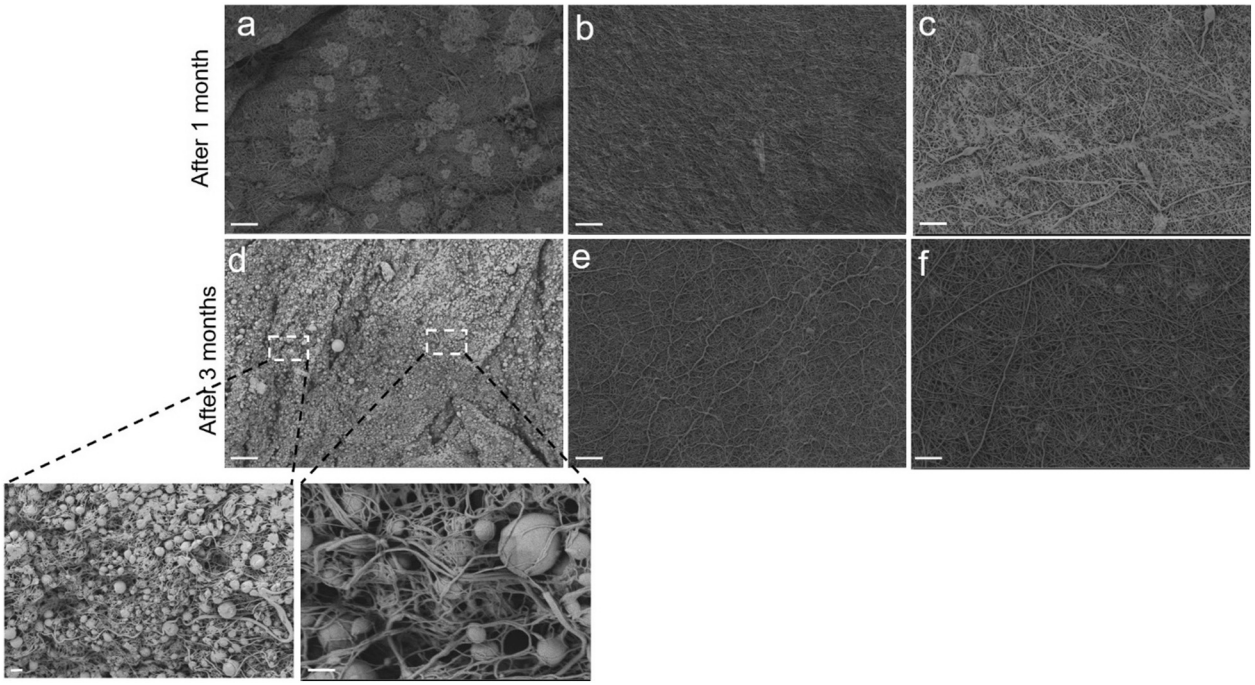

Fig. 4. SEM images of PCL (a & d), 1 wt% BSA/PCL (b & e), and 3 wt% BSA/PCL nanofibers (c & f) following 1 and 3 months immersion in PBS to characterize their hydrolytic degradation (the scale bars in a-f represent 20 μm and the scale bars in the inset images of d represent 3 μm (left) and 1 μm (right), respectively). The largest degradation level is seen for the PCL nanofibers, while the biohybrid nanofibers seem durable even after three months. The whitish precipitate seen on the surface of the biohybrid nanofiber mat (c) is assumed to be related to deposition of the salts present in PBS, that are re-dissolved after 3 months (f).

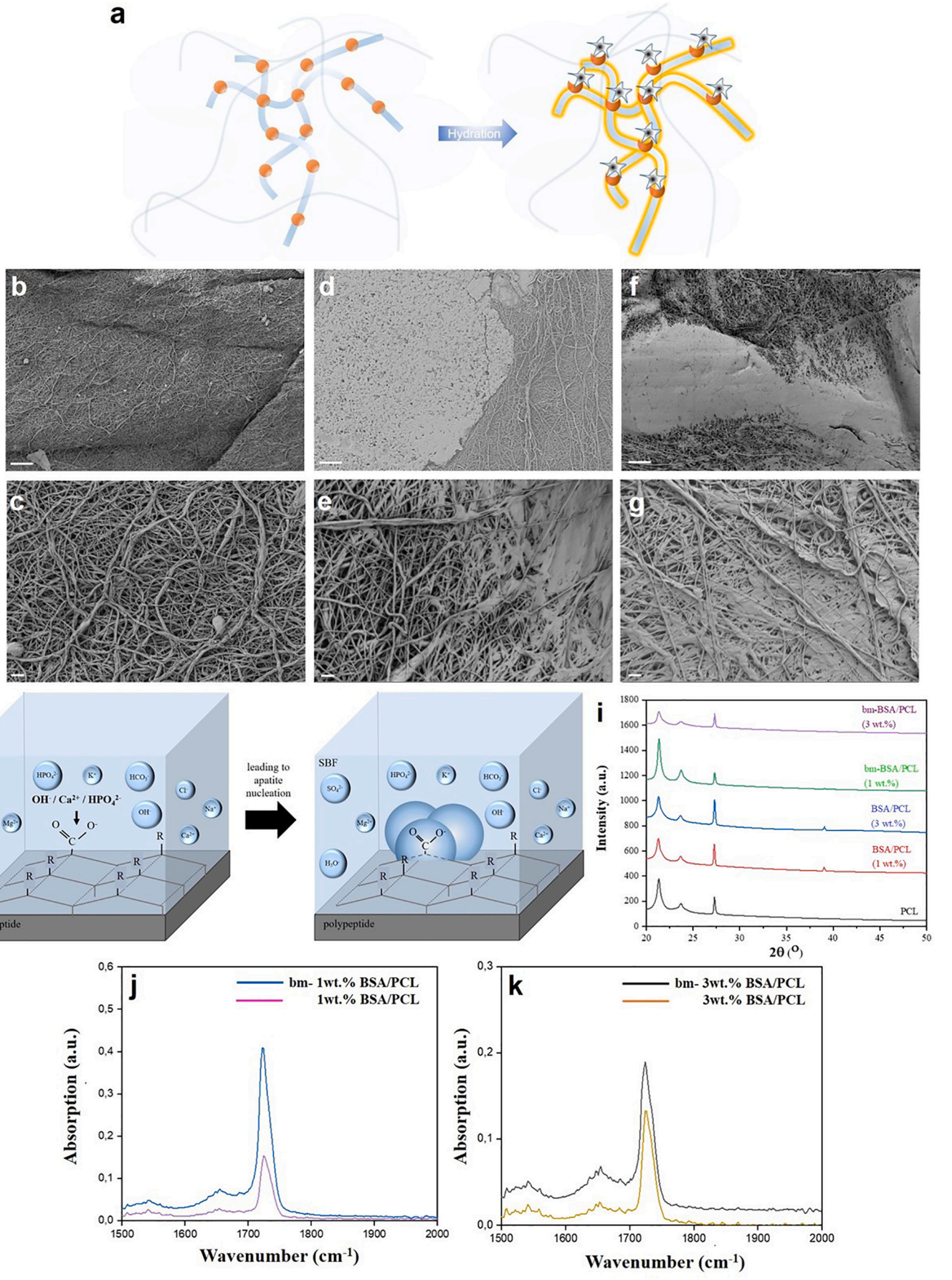

(caption on next page)

Fig. 5. a) Schematic illustration of the biohybrid nanofibers containing BSA (marked by orange circles). BSA's conformational status changes from folded (α-helix) to unfolded (β-sheet) upon exposure to aqueous media, thereby interacting with cells and ions (biomineralization; represented by an orange shell) more efficiently. SEM images indicate the absence of biominerals on the surface of the neat PCL nanofiber mat (b & c) versus the presence of a large fraction of biominerals covering the surface of the biohybrid nanofiber mats (d & e for 1 wt.% BSA/PCL and f & g for 3 wt.% BSA/PCL) in different magnifications (the scale bars in b-g represent 20 μm). h) Schematic illustration of the biomineralization process on the protein segments of the biohybrid nanofibers, where the functional groups initiate nucleation of the biominerals. The schematic was re-drawn based on a similar one in [75]. i) XRD spectra compare the crystalline characteristic peaks of the biohybrid nanofibers before and after immersion in SBF. The XRD analysis shows that the formed biomineral is amorphous in nature. j & k) ATR-FTIR graphs for the biohybrid nanofibers (containing 1 and 3 wt% BSA) before and after biomineralization (represented by the "bm" prefix).

cysteine residue groups that could interact with Ca^{2+}, are mainly concealed inside the protein structure and not available [52,72]. In addition, there is a robust hydrogen bond between the peptide groups, that limits exposure of the amine groups. In contrast, upon increase of the pH to neutral, BSA's conformational state is transformed to β-sheet with exposed functional groups. As a result, the carboxyl and phosphorous groups of BSA achieve largely negative dipoles able to chelate the free Ca^{2+} cations in the SBF [73] and to initiate biomineralization. On the other hand, HPO_4^{2-} ions bond with the protein-reduced calcium, thereby generating a calcium phosphate compound [74]. This could be the case for formation of calcium carbonate when instead of HPO_4^{2-}, HCO_3^- ions react with the reduced calcium nuclei. Fig. 5j & k shows the

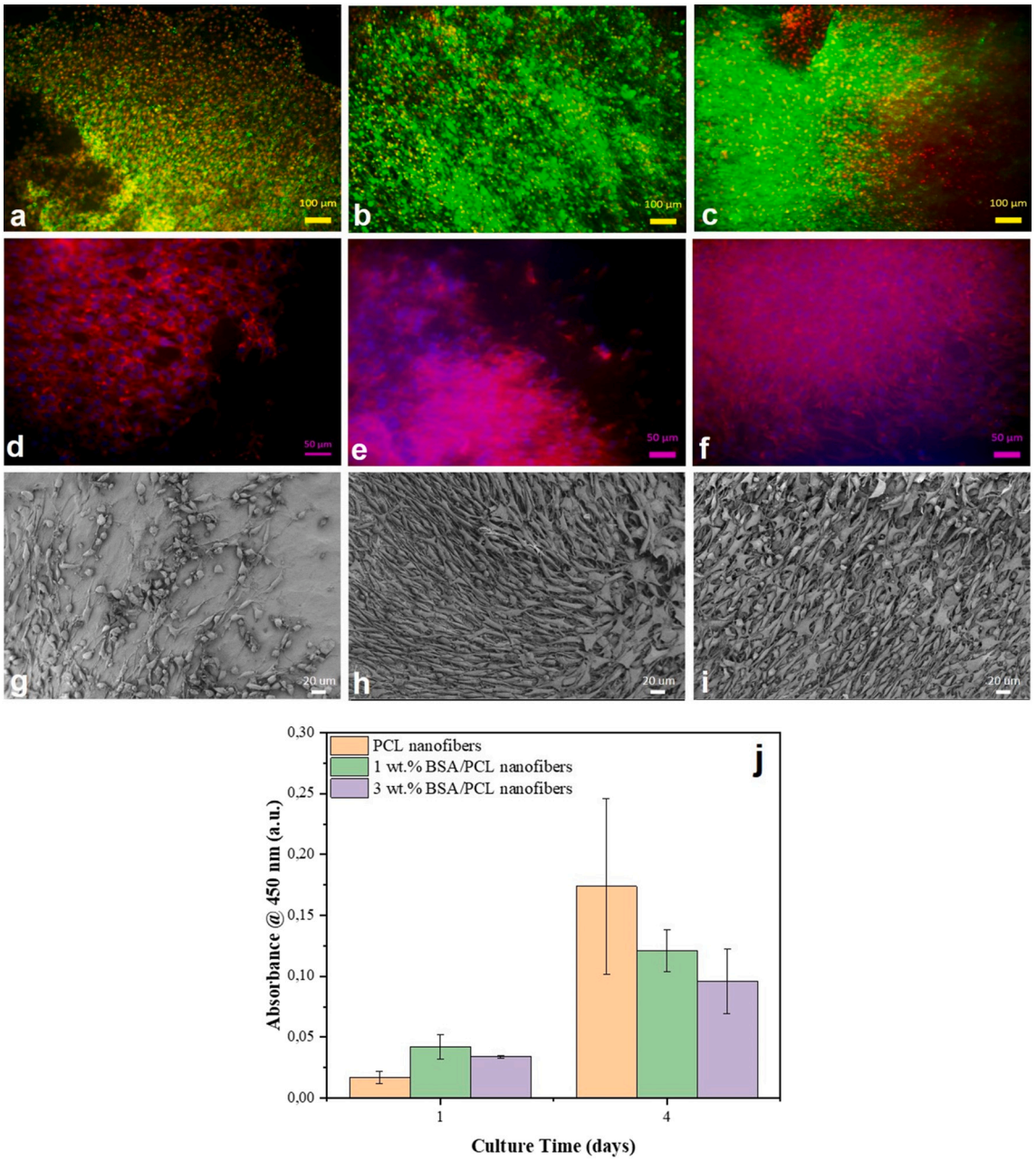

Fig. 6. NIH 3T3 cell viability and morphology monitored through the live-dead assay (a–c), phalloidin/DAPI assay (d–f) and SEM (g–i) for the cells seeded on the nanofiber mats composed of PCL (a, d, and g), 1 wt% BSA/PCL (b, e, and h), and 3 wt% BSA/PCL (c, f, and i) after 4 days. j) Viability of the NIH 3T3 cells co-cultured with the biohybrid nanofiber mats after 1 and 4 days. No significant difference ($p < 0.05$) was recorded between the cell viability data after 4 days.

characteristic amide peaks of BSA, representing the α-helix structure of the protein after biomineralization in the dry state. Interestingly, the peaks intensity increases after biomineralization, implying that a larger number of BSA molecules and their functional groups have been involved in the process. This result is an indication of the conformational change of the BSA molecules and their higher mobility, ending up with more interaction with the cations available in SBF during the biomineralization process.

The identity of the formed biomineral was unraveled by XRD and EDX. As shown in Fig. 5i, the characteristic peaks of PCL appear at 2θ of 21° and 24° that are attributed to (110) and (200) orthorhombic crystallographic planes, respectively [76]. The additional peak appearing at 2θ of 27° could be related to recrystallization of the PCL chains during electrospinning [77]. Such a behavior has already been reported by Stephens et al. [78] for electrospun nylon nanofibers. The mentioned peaks persist for the biohybrid nanofibers, while a new peak also emerges at 2θ of 38° that could be caused by crystallization of BSA. BSA and PCL in the blend solution show totally different behavior in terms of hydrophilicity. In contrast to PCL, BSA is hydrophilic and this feature ends up with its partial crystallization. Moreover, the higher solubility of BSA in the applied solvents leads to diffusive transport of the protein towards the nanofiber surface during electrospinning and jet solidification and thus raises the chance of BSA crystallization. Salem et al. [79] report a similar observation when a hydrophilic drug such as caffeine is blended with hydrophobic PCL in a nanofibrous system. It is worthy to note that the typical crystalline peaks of BSA emerge at 2θ of 9° and 20° [80] which are different than the peak we recorded for the biohybrid nanofibers. Lastly, the biomineralized nanofibers show only the characteristic peaks of PCL, implying the amorphous nature of the biominerals formed and amorphization of the protein segments. The composition of the biomineral layer was determined by EDX analysis. As shown in Fig. S3a–c, the biomineral is almost free of phosphorus and is mainly composed of C, O, and Ca. As a conclusion, the biomineral covering the surface of the biohybrid nanofiber mats is made of amorphous calcium carbonate.

The biohybrid nanofibers developed in our study comprise a PCL matrix with scattered BSA domains. While biocompatibility of PCL has been already widely validated in the literature [81,82], biological (cell) behavior of the BSA/PCL blend nanofibers has never been studied to the best of our knowledge. Fig. 6a–c shows the cell adhesion on the nanofiber mats and the population of live and dead cells (represented by green and red spots, respectively) after 4 days incubation. The cells present on the PCL nanofiber mat are less proliferative as compared to those on the biohybrid mats and even a number of dead cells are visible on the surface. The reason for less cell adhesion on the PCL nanofiber surface could be associated to its hydrophobicity and slight negative charge. PCL nanofibers show an isoelectric point of ~4 [83], therefore within the physiological medium they could show a negative surface charge. Given the fact that the cells' membrane is negatively charged, an electrostatic repulsion between the PCL nanofibers and the cells is plausible. A much larger population of the cells adheres onto the biohybrid nanofiber mats in comparison to the neat PCL one and it seems that they are aligned along the nanofibers. In the case of the biohybrid nanofiber mat containing 3 wt% BSA, the extremely dense colonies of the cells could even lead to death of some cells.

The phalloidin/DAPI assay results further stress the notable tendency of the cells to adhere on the biohybrid nanofiber mats compared to the PCL one, Fig. 6d–f. SEM images, Fig. 6g–i, also clearly demonstrate that the cells stick to the surface of the biohybrid mats at much larger densities. Interestingly, the shape of the cells adhered on the surface of the nanofiber mats is quite different. While the cells are stretched and expanded on the biohybrid mats, they remain spherical and isolated in different areas of the PCL nanofiber mat. Surprisingly, the WST-8 data, Fig. 6j, imply that the PCL nanofibers have been more encouraging towards proliferation of the cells after 4 days.

The cell adhesion and shape are strongly associated with the nanoscale topography of the substrates [84]. In this regard, likely partial dissolution and release of BSA into the culture medium could lead to higher roughness of the nanofiber surface, thus providing a better platform for adhesion of the cells. Moreover, the presence of BSA on the surface and its conformational change upon hydration, leading to exposure and protonation of amine groups, confer a positively charged surface to the biohybrid nanofibers. It is worthy to note that in a cell culture, pH fluctuation is an inevitable consequence of cell metabolism and generally the cell medium shifts to acidic conditions [85]. This feature will end up with protonation of the amine groups of BSA. Taking into account that the cell membrane has a net negative charge, electrostatic interactions between the cells and the biohybrid nanofibers play an important role in their extensive adhesion. Such a behavior has been already reported by Kim et al. [86]. As they have shown, NIH 3T3 cells adhere up to 20% more on positively charged PCL substrates than on the negatively charged counterpart. Moreover, surface of the biohybrid nanofiber mats adsorb serum proteins, thus impacting adhesion of the cells positively. This behavior is in harmony with the results reported by Keselowsky et al. [87]. They state that fibronectin adheres preferably on the surfaces functionalized with amine groups among others with the order of $NH_3^+ > CH_3 > COO^- > OH$. Fibronectin provides specific binding sites for adhesion-mediating proteins in the cells' membrane, i.e. integrins.

The morphology of the adhered cells depends strongly on the surface charge. The cells adhered on the positively charged surface of the biohybrid nanofibers adopt a flattened shape, while the cells on the PCL nanofiber mat remain round and in a narrow shape. A similar performance has been reported by Kim et al. [86]. The cell shape could be decisive in determining the cell function [88]. For instance, Li et al. [89] state that highly elongated (flattened) fibroblast cells (as the cells adhered on the BSA/PCL nanofiber mat) showed 40% larger collagen type I expression in comparison with the circular fibroblast cells (as the cells adhered on the PCL nanofiber mat).

The proliferation of the NIH 3T3 cells significantly rises when co-cultured with the PCL (920%) and the biohybrid nanofibers (190% and 182% for the nanofibers containing 1 and 3 wt% BSA, respectively) after 4 days. It is assumed that BSA can be released into the cell culture, thereby promoting metabolism of the cells and their proliferation. This can lead to reaching the proliferation peak in a shorter time than 4 days as well as acidification of the medium. Both these consequences could reduce further proliferation of the cells and even result in their death after the peak. Therefore, after 4 days, the number of the cells co-cultured with the PCL nanofibers prevails over that incubated with the biohybrid nanofibers. The positive effect of BSA on proliferation of the preosteoblast cells has been already reported by Zhu et al. [90]. The higher proliferation rate of the cells cultured alongside the biohybrid nanofibers is indeed promising and implies that a wound can be healed faster when treated with the biohybrid nanofibers.

4. Conclusion

In this study, BSA as a commercial, inexpensive biomacromolecule was employed as a blending agent to address the limitations of PCL nanofiber mats for wound dressing applications, including mechanical weakness and lack of bioactivity. From the mechanical standpoint, elasticity and elongation of the PCL nanofibers were notably enhanced after BSA inclusion. The presence of BSA also stimulated cell adhesion and growth on the surface of the nanofiber mats. Conclusively, BSA is able to improve mechanobiological properties of PCL nanofiber mats and allows us to propose this combination for wound dressing applications.

CRediT authorship contribution statement

Shahin Homaeigohar: Conceptualization, Methodology, Validation, Formal analysis, Investigation, Writing - original draft, Writing -

review & editing, Visualization, Supervision, Funding acquisition. **Mahshid Monavari:** Validation, Investigation. **Benedict Koenen:** Investigation. **Aldo R. Boccaccini:** Writing - review & editing, Resources, Funding acquisition.

Declaration of competing interest

The authors declare that they have no known competing financial interests or personal relationships that could have appeared to influence the work reported in this paper.

Acknowledgement

S.H. and A.R.B. would like to acknowledge the financial support received from the European Union's Horizon 2020 - Research and Innovation Program under the Marie Skłodowska-Curie grant agreement No. 839165.

Appendix A. Supplementary data

Supplementary data to this article can be found online at https://doi.org/10.1016/j.msec.2021.111965.

References

[1] R. Raman, R. Langer, Biohybrid design gets personal: new materials for patient-specific therapy, Adv. Mater. 32 (2020), 1901969.
[2] A. Yari Sadi, M.A. Shokrgozar, S.S. Homaeigohar, A. Khavandi, Biological evaluation of partially stabilized zirconia added HA/HDPE composites with osteoblast and fibroblast cell lines, J. Mater. Sci. Mater. Med. 19 (6) (2008) 2359–2365.
[3] S.S. Homaeigohar, M. Shokrgozar, J. Javadpour, A. Khavandi, A.Y. Sadi, Effect of reinforcement particle size on in vitro behavior of β-tricalcium phosphate-reinforced high-density polyethylene: a novel orthopedic composite, J. Biomed. Mater. Res. A 78 (1) (2006) 129–138.
[4] A. Martins, J.V. Araújo, R.L. Reis, N.M. Neves, Electrospun Nanostructured Scaffolds for Tissue Engineering Applications, 2007.
[5] R.G. Flemming, C.J. Murphy, G.A. Abrams, S.L. Goodman, P.F. Nealey, Effects of synthetic micro-and nano-structured surfaces on cell behavior, biomaterials 20 (6) (1999) 573–588.
[6] T.G. Kim, T.G. Park, Biomimicking extracellular matrix: cell adhesive RGD peptide modified electrospun poly (D, L-lactic-co-glycolic acid) nanofiber mesh, Tissue Eng. 12 (2) (2006) 221–233.
[7] W. Jia, M. Li, L. Kang, G. Gu, Z. Guo, Z. Chen, Fabrication and comprehensive characterization of biomimetic extracellular matrix electrospun scaffold for vascular tissue engineering applications, J. Mater. Sci. 54 (15) (2019) 10871–10883.
[8] Y. Zhu, D. Wang, X. Yao, M. Wang, Y. Zhao, Y. Lu, Z. Wang, Y. Guo, Biomimetic hybrid scaffold of electrospun silk fibroin and pancreatic decellularized extracellular matrix for islet survival, Journal of Biomaterials Science, Polymer Edition (2020) 1–16 (just-accepted).
[9] S. Homaeigohar, T.-Y. Tsai, E.S. Zarie, M. Elbahri, T.-H. Young, A.R. Boccaccini, Bovine Serum Albumin (BSA)/polyacrylonitrile (PAN) biohybrid nanofibers coated with a biomineralized calcium deficient hydroxyapatite (HA) shell for wound dressing, Mater. Sci. Eng. C 116 (2020), 111248.
[10] M. Abrigo, S.L. McArthur, P. Kingshott, Electrospun nanofibers as dressings for chronic wound care: advances, challenges, and future prospects, Macromol. Biosci. 14 (6) (2014) 772–792.
[11] P. Sawadkar, J. Mohanakrishnan, P. Rajasekar, B. Rahmani, N. Kohli, L. Bozec, E. García-Gareta, A synergistic relationship between polycaprolactone and natural polymers enhances the physical properties and biological activity of scaffolds, ACS Appl. Mater. Interfaces 12 (12) (2020) 13587–13597.
[12] S. Homaeigohar, T.-Y. Tsai, T.-H. Young, H.J. Yang, Y.-R. Ji, An electroactive alginate hydrogel nanocomposite reinforced by functionalized graphite nanofilaments for neural tissue engineering, Carbohydr. Polym. 224 (2019) 115112.
[13] S. Homaeigohar, A.R. Boccaccini, Antibacterial biohybrid nanofibers for wound dressings, Acta Biomater. 107 (2020) 25–49.
[14] C.-H. Yao, C.-Y. Lee, C.-H. Huang, Y.-S. Chen, K.-Y. Chen, Novel bilayer wound dressing based on electrospun gelatin/keratin nanofibrous mats for skin wound repair, Mater. Sci. Eng. C 79 (2017) 533–540.
[15] P. Wutticharoenmongkol, P. Hannirojram, P. Nuthong, Gallic acid-loaded electrospun cellulose acetate nanofibers as potential wound dressing materials, Polym. Adv. Technol. 30 (4) (2019) 1135–1147.
[16] G. Perumal, S. Pappuru, D. Chakraborty, A.M. Nandkumar, D.K. Chand, M. Doble, Synthesis and characterization of curcumin loaded PLA—Hyperbranched polyglycerol electrospun blend for wound dressing applications, Mater. Sci. Eng. C 76 (2017) 1196–1204.
[17] B. Guo, P.X. Ma, Synthetic biodegradable functional polymers for tissue engineering: a brief review, SCIENCE CHINA Chem. 57 (4) (2014) 490–500.
[18] G. Jin, M.P. Prabhakaran, D. Kai, M. Kotaki, S. Ramakrishna, Electrospun photosensitive nanofibers: potential for photocurrent therapy in skin regeneration, Photochem. Photobiol. Sci. 12 (1) (2013) 124–134.
[19] K.W. Ng, H.N. Achuth, S. Moochhala, T.C. Lim, D.W. Hutmacher, In vivo evaluation of an ultra-thin polycaprolactone film as a wound dressing, J. Biomater. Sci. Polym. Ed. 18 (7) (2007) 925–938.
[20] Y. Huang, N. Dan, W. Dan, W. Zhao, Reinforcement of polycaprolactone/chitosan with nanoclay and controlled release of curcumin for wound dressing, ACS Omega 4 (27) (2019) 22292–22301.
[21] Z. Muwaffak, A. Goyanes, V. Clark, A.W. Basit, S.T. Hilton, S. Gaisford, Patient-specific 3D scanned and 3D printed antimicrobial polycaprolactone wound dressings, Int. J. Pharm. 527 (1) (2017) 161–170.
[22] E.Y. Teo, S.-Y. Ong, M.S. Khoon Chong, Z. Zhang, J. Lu, S. Moochhala, B. Ho, S.-H. Teoh, Polycaprolactone-based fused deposition modeled mesh for delivery of antibacterial agents to infected wounds, Biomaterials 32 (1) (2011) 279–287.
[23] M. Li, J. Chen, M. Shi, H. Zhang, P.X. Ma, B. Guo, Electroactive anti-oxidant polyurethane elastomers with shape memory property as non-adherent wound dressing to enhance wound healing, Chem. Eng. J. 375 (2019) 121999.
[24] K. Fox, P.A. Tran, D.W.M. Lau, T. Ohshima, A.D. Greentree, B.C. Gibson, Nanodiamond-polycaprolactone composite: a new material for tissue engineering with sub-dermal imaging capabilities, Mater. Lett. 185 (2016) 185–188.
[25] M. Heidari, S.H. Bahrami, M. Ranjbar-Mohammadi, P. Milan, Smart electrospun nanofibers containing PCL/gelatin/graphene oxide for application in nerve tissue engineering, Mater. Sci. Eng. C 103 (2019) 109768.
[26] M.A. Nazeer, E. Yilgor, I. Yilgor, Electrospun polycaprolactone/silk fibroin nanofibrous bioactive scaffolds for tissue engineering applications, Polymer 168 (2019) 86–94.
[27] L. Wang, Y. Wu, B. Guo, P.X. Ma, Nanofiber yarn/hydrogel core–shell scaffolds mimicking native skeletal muscle tissue for guiding 3D myoblast alignment, elongation, and differentiation, ACS Nano 9 (9) (2015) 9167–9179.
[28] Y. Wu, L. Wang, B. Guo, P.X. Ma, Interwoven aligned conductive nanofiber yarn/hydrogel composite scaffolds for engineered 3D cardiac anisotropy, ACS Nano 11 (6) (2017) 5646–5659.
[29] D. Shin, M.S. Kim, C.E. Yang, W.J. Lee, T.S. Roh, W. Baek, Radially patterned polycaprolactone nanofibers as an active wound dressing agent, Arch. Plast. Surg. 46 (5) (2019) 399.
[30] M. Suryamathi, C. Ruba, P. Viswanathamurthi, V. Balasubramanian, P. Perumal, Tridax procumbens extract loaded electrospun PCL nanofibers: a novel wound dressing material, Macromol. Res. 27 (1) (2019) 55–60.
[31] V. Leszczak, K.C. Popat, Improved in vitro blood compatibility of polycaprolactone nanowire surfaces, ACS Appl. Mater. Interfaces 6 (18) (2014) 15913–15924.
[32] Y. Ji, K. Liang, X. Shen, G.L. Bowlin, Electrospinning and characterization of chitin nanofibril/polycaprolactone nanocomposite fiber mats, Carbohydr. Polym. 101 (2014) 68–74.
[33] J.I. Choi, M.S. Kim, G.Y. Chung, H.S. Shin, Spirulina extract-impregnated alginate-PCL nanofiber wound dressing for skin regeneration, Biotechnol. Bioprocess Eng. 22 (6) (2017) 679–685.
[34] S.J. Lee, J. Liu, S.H. Oh, S. Soker, A. Atala, J.J. Yoo, Development of a composite vascular scaffolding system that withstands physiological vascular conditions, Biomaterials 29 (19) (2008) 2891–2898.
[35] J. He, Y. Liang, M. Shi, B. Guo, Anti-oxidant electroactive and antibacterial nanofibrous wound dressings based on poly(ε-caprolactone)/quaternized chitosan-graft-polyaniline for full-thickness skin wound healing, Chem. Eng. J. 385 (2020) 123464.
[36] J.H. Jo, E.J. Lee, D.S. Shin, H.E. Kim, H.W. Kim, Y.H. Koh, J.H. Jang, In vitro/in vivo biocompatibility and mechanical properties of bioactive glass nanofiber and poly (ε-caprolactone) composite materials, J. Biomed. Mater. Res. B Appl. Biomater. 91 (1) (2009) 213–220.
[37] J.-P. Chen, Y.-S. Chang, Preparation and characterization of composite nanofibers of polycaprolactone and nanohydroxyapatite for osteogenic differentiation of mesenchymal stem cells, Colloids Surf. B: Biointerfaces 86 (1) (2011) 169–175.
[38] M. Diba, M. Fathi, M. Kharaziha, Novel forsterite/polycaprolactone nanocomposite scaffold for tissue engineering applications, Mater. Lett. 65 (12) (2011) 1931–1934.
[39] A.G.B. Castro, M. Diba, M. Kersten, J.A. Jansen, J.J.J.P. van den Beucken, F. Yang, Development of a PCL-silica nanoparticles composite membrane for guided bone regeneration, Mater. Sci. Eng. C 85 (2018) 154–161.
[40] T. Wu, X. Chen, J. Sha, Y.-Y. Peng, Y.-L. Ma, L.-S. Xie, L.-S. Turng, Fabrication of shish-kebab-structured carbon nanotube/poly (ε-caprolactone) composite nanofibers for potential tissue engineering applications, Rare Metals 38 (1) (2019) 64–72.
[41] S.Sh Homaeigohar, H. Mahdavi, M. Elbahri, Extraordinarily water permeable sol gel formed nanocomposite nanofibrous membranes, J. Colloid Interface Sci. 366 (2012) 51–56.
[42] M.S. Kim, G. Kim, Three-dimensional electrospun polycaprolactone (PCL)/alginate hybrid composite scaffolds, Carbohydr. Polym. 114 (2014) 213–221.
[43] M. Singh, H. Chand, K.C. Gupta, The studies of density, apparent molar volume, and viscosity of bovine serum albumin, egg albumin, and lysozyme in aqueous and RbI, CsI, and DTAB aqueous solutions at 303.15 K, Chem. Biodivers. 2 (6) (2005) 809–824.
[44] S.J. Eichhorn, W.W. Sampson, Statistical geometry of pores and statistics of porous nanofibrous assemblies, J. R. Soc. Interface 2 (4) (2005) 309–318.

[45] L.L. Lima, T.B. Taketa, M.M. Beppu, I.M.d.O. Sousa, M.A. Foglio, Â.M. Moraes, Coated electrospun bioactive wound dressings: mechanical properties and ability to control lesion microenvironment, Mater. Sci. Eng. C 100 (2019) 493–504.
[46] T. Kokubo, H. Takadama, How useful is SBF in predicting in vivo bone bioactivity? Biomaterials 27 (15) (2006) 2907–2915.
[47] C.-H. Park, C.-H. Kim, L.D. Tijing, D.-H. Lee, M.-H. Yu, H.R. Pant, Y. Kim, C.S. Kim, Preparation and characterization of (polyurethane/nylon-6) nanofiber/(silicone) film composites via electrospinning and dip-coating, Fibers Polym. 13 (3) (2012) 339–345.
[48] N.S. Sambudi, M.G. Kim, S.B. Park, The formation of web-like connection among electrospun chitosan/PVA fiber network by the reinforcement of ellipsoidal calcium carbonate, Mater. Sci. Eng. C 60 (2016) 518–525.
[49] S. Natarajan, D. Williamson, A.J. Stiltz, K. Harding, Advances in wound care and healing technology, Am. J. Clin. Dermatol. 1 (5) (2000) 269–275.
[50] X. Hu, K. Shmelev, L. Sun, E.-S. Gil, S.-H. Park, P. Cebe, D.L. Kaplan, Regulation of silk material structure by temperature-controlled water vapor annealing, Biomacromolecules 12 (5) (2011) 1686–1696.
[51] P.J. Flory, Principles of Polymer Chemistry, Cornell University Press, 1953.
[52] M. Elbahri, T. Dai Sh. Homaeigohar, R. Abdelaziz, R. Khalil, A.U. Zillohu, Smart metal-polymer bionanocomposites as omnidirectional plasmonic black absorbers formed by, Nanofluid Filtr. Adv. Funct. Mater. 22 (22) (2012) 4771–4777.
[53] S. Homaeigohar, T. Dai, M. Elbahri, Biofunctionalized nanofibrous membranes as super separators of protein and enzyme from water, J. Colloid Interface Sci. 406 (0) (2013) 86–93.
[54] S. Homaeigohar, D. Disci-Zayed, T. Dai, M. Elbahri, Biofunctionalized nanofibrous membranes mimicking carnivorous plants, Bioinspired, Biomim. Nanobiomater. 2 (4) (2013) 186–193.
[55] I. Rombouts, B. Lagrain, K.A. Scherf, M.A. Lambrecht, P. Koehler, J.A. Delcour, Formation and reshuffling of disulfide bonds in bovine serum albumin demonstrated using tandem mass spectrometry with collision-induced and electron-transfer dissociation, Sci. Rep. 5 (2015), 12210.
[56] C. Guo, X. Guo, W. Chu, N. Jiang, H. Li, Spectroscopic study of conformation changes of bovine serum albumin in aqueous environment, Chin. Chem. Lett. 30 (6) (2019) 1302–1306.
[57] Z. Fereshteh, M.H. Fathi, R. Mozaffarinia, Mg-doped fluorapatite nanoparticles-poly(ε-caprolactone) electrospun nanocomposite: microstructure and mechanical properties, Superlattice. Microst. 75 (2014) 208–221.
[58] Z. Heydari, D. Mohebbi-Kalhori, M.S. Afarani, Engineered electrospun polycaprolactone (PCL)/octacalcium phosphate (OCP) scaffold for bone tissue engineering, Mater. Sci. Eng. C 81 (2017) 127–132.
[59] I. Rajzer, E. Menaszek, R. Kwiatkowski, J.A. Planell, O. Castano, Electrospun gelatin/poly(ε-caprolactone) fibrous scaffold modified with calcium phosphate for bone tissue engineering, Mater. Sci. Eng. C 44 (2014) 183–190.
[60] R.M. Aghdam, S. Najarian, S. Shakhesi, S. Khanlari, K. Shaabani, S. Sharifi, Investigating the effect of PGA on physical and mechanical properties of electrospun PCL/PGA blend nanofibers, J. Appl. Polym. Sci. 124 (1) (2012) 123–131.
[61] C. Wan, B. Chen, Poly (ε-caprolactone)/graphene oxide biocomposites: mechanical properties and bioactivity, Biomed. Mater. 6 (5) (2011) 055010.
[62] D. Chouhan, B. Chakraborty, S.K. Nandi, B.B. Mandal, Role of non-mulberry silk fibroin in deposition and regulation of extracellular matrix towards accelerated wound healing, Acta Biomater. 48 (2017) 157–174.
[63] R. Xu, G. Luo, H. Xia, W. He, J. Zhao, B. Liu, J. Tan, J. Zhou, D. Liu, Y. Wang, Novel bilayer wound dressing composed of silicone rubber with particular micropores enhanced wound re-epithelialization and contraction, Biomaterials 40 (2015) 1–11.
[64] M.M. Stevens, J.H. George, Exploring and engineering the cell surface interface, Science 310 (5751) (2005) 1135–1138.
[65] F. Sun, H.R. Nordli, B. Pukstad, E. Kristofer Gamstedt, G. Chinga-Carrasco, Mechanical characteristics of nanocellulose-PEG bionanocomposite wound dressings in wet conditions, J. Mech. Behav. Biomed. Mater. 69 (2017) 377–384.
[66] G. Josefsson, P. Ahvenainen, N.E. Mushi, E.K. Gamstedt, Fibril orientation redistribution induced by stretching of cellulose nanofibril hydrogels, J. Appl. Phys. 117 (21) (2015) 214311.
[67] K.L. Spence, R.A. Venditti, O.J. Rojas, Y. Habibi, J.J. Pawlak, The effect of chemical composition on microfibrillar cellulose films from wood pulps: water interactions and physical properties for packaging applications, Cellulose 17 (4) (2010) 835–848.
[68] A. Vasconcelos, A. Cavaco-Paulo, Wound dressings for a proteolytic-rich environment, Appl. Microbiol. Biotechnol. 90 (2) (2011) 445–460.
[69] T. Kokubo, H. Kushitani, S. Sakka, T. Kitsugi, T. Yamamuro, Solutions able to reproduce in vivo surface-structure changes in bioactive glass-ceramic A-W3, J. Biomed. Mater. Res. 24 (6) (1990) 721–734.
[70] N. Goonoo, B. Khanbabaee, M. Steuber, A. Bhaw-Luximon, U. Jonas, U. Pietsch, D. Jhurry, H. Schönherr, κ-Carrageenan enhances the biomineralization and osteogenic differentiation of electrospun polyhydroxybutyrate and polyhydroxybutyrate valerate fibers, Biomacromolecules 18 (5) (2017) 1563–1573.
[71] N. El Kadi, N. Taulier, J. Le Huerou, M. Gindre, W. Urbach, I. Nwigwe, P. Kahn, M. Waks, Unfolding and refolding of bovine serum albumin at acid pH: ultrasound and structural studies, Biophys. J. 91 (9) (2006) 3397–3404.
[72] D. Zhang, O. Neumann, H. Wang, V.M. Yuwono, A. Barhoumi, M. Perham, J. D. Hartgerink, P. Wittung-Stafshede, N.J. Halas, Gold nanoparticles can induce the formation of protein-based aggregates at physiological pH, Nano Lett. 9 (2) (2009) 666–671.
[73] T. Kokubo, H.-M. Kim, M. Kawashita, Novel bioactive materials with different mechanical properties, Biomaterials 24 (13) (2003) 2161–2175.
[74] H. Zhao, W. He, Y. Wang, X. Zhang, Z. Li, S. Yan, W. Zhou, G. Wang, Biomineralization of large hydroxyapatite particles using ovalbumin as biosurfactant, Mater. Lett. 62 (20) (2008) 3603–3605.
[75] A. Takeuchi, C. Ohtsuki, T. Miyazaki, M. Kamitakahara, S.-i Ogata, M. Yamazaki, Y. Furutani, H. Kinoshita, M. Tanihara, Heterogeneous nucleation of hydroxyapatite on protein: structural effect of silk sericin, J. R. Soc. Interface 2 (4) (2005) 373–378.
[76] A. Baji, S.C. Wong, T. Liu, T. Li, T. Srivatsan, Morphological and X-ray diffraction studies of crystalline hydroxyapatite-reinforced polycaprolactone, J. Biomed. Mater. Res B Appl. Biomater. 81 (2) (2007) 343–350.
[77] J.E. Oliveira, L.H. Mattoso, W.J. Orts, E.S. Medeiros, Structural and morphological characterization of micro and nanofibers produced by electrospinning and solution blow spinning: a comparative study, Adv. Mater. Sci. Eng. 2013 (2013).
[78] J.S. Stephens, D.B. Chase, J.F. Rabolt, Effect of the electrospinning process on polymer crystallization chain conformation in nylon-6 and nylon-12, Macromolecules 37 (3) (2004) 877–881.
[79] S. Seif, L. Franzen, M. Windbergs, Overcoming drug crystallization in electrospun fibers – elucidating key parameters and developing strategies for drug delivery, Int. J. Pharm. 478 (1) (2015) 390–397.
[80] M.W. Sabaa, D.H. Hanna, M.H.A. Elella, R.R. Mohamed, Encapsulation of bovine serum albumin within novel xanthan gum based hydrogel for protein delivery, Mater. Sci. Eng. C 94 (2019) 1044–1055.
[81] Y.Z. Zhang, J. Venugopal, Z.M. Huang, C.T. Lim, S. Ramakrishna, Characterization of the surface biocompatibility of the electrospun PCL-collagen nanofibers using fibroblasts, Biomacromolecules 6 (5) (2005) 2583–2589.
[82] M.K. Joshi, A.P. Tiwari, H.R. Pant, B.K. Shrestha, H.J. Kim, C.H. Park, C.S. Kim, In situ generation of cellulose nanocrystals in polycaprolactone nanofibers: effects on crystallinity, mechanical strength, biocompatibility, and biomimetic mineralization, ACS Appl. Mater. Interfaces 7 (35) (2015) 19672–19683.
[83] S. Metwally, S. Ferraris, S. Spriano, Z.J. Krysiak, Ł. Kaniuk, M.M. Marzec, S.K. Kim, P.K. Szewczyk, A. Gruszczyński, M. Wytrwal-Sarna, J.E. Karbowniczek, A. Bernasik, S. Kar-Narayan, U. Stachewicz, Surface potential and roughness controlled cell adhesion and collagen formation in electrospun PCL fibers for bone regeneration, Mater. Des. 194 (2020) 108915.
[84] T. Dvir, B.P. Timko, D.S. Kohane, R. Langer, Nanotechnological strategies for engineering complex tissues, Nat. Nanotechnol. 6 (1) (2011) 13.
[85] J. Michl, K.C. Park, P. Swietach, Evidence-based guidelines for controlling pH in mammalian live-cell culture systems, Commun. Biol. 2 (1) (2019) 144.
[86] J. Kim, D.-H. Kim, K.T. Lim, H. Seonwoo, S.H. Park, Y.-R. Kim, Y. Kim, Y.-H. Choung, P.-H. Choung, J.H. Chung, Charged nanomatrices as efficient platforms for modulating cell adhesion and shape, Tissue Eng. C Methods 18 (12) (2012) 913–923.
[87] B.G. Keselowsky, D.M. Collard, A.J. García, Surface chemistry modulates focal adhesion composition and signaling through changes in integrin binding, Biomaterials 25 (28) (2004) 5947–5954.
[88] M. Hirata, M. Kobayashi, C. Matsumoto, C. Miyaura, T. Asakura, M. Inada, Cell shape and matrix production of fibroblasts cultured on fibroin-organized silk scaffold with type-II β-turn structured (Ala-Gly-Ala-Gly-Ser-Gly) n sequences, J. Health Sci. 56 (6) (2010) 738–744.
[89] F. Li, B. Li, Q.M. Wang, J.H.C. Wang, Cell shape regulates collagen type I expression in human tendon fibroblasts, Cell Motil. Cytoskeleton 65 (4) (2008) 332–341.
[90] Y. Zhu, L. Yao, Z. Liu, W. Weng, K. Cheng, Electrical potential specified release of BSA/Hep/polypyrrole composite film and its cellular responses, ACS Appl. Mater. Interfaces 11 (28) (2019) 25457–25464.